energies

MDPI

Article

An Experimental Study of Boiling Heat Transfer and Quench Front Propagation Velocity During Quenching of a Cylinder Rod in Subcooled Water

Yuanyang Sun [1], Huanyan Jian [2], Ping Xiong [1,*] and Linglan Zhou [1]

[1] Key Laboratory of Fluid and Power Machinery, Xihua University, Pidu District, Chengdu 610039, China; syy19102826702@sina.com (Y.S.); 0120240026@xhu.edu.cn (L.Z.)
[2] School of Computer Science and Engineering, Southwest Minzu University, Shuangliu District, Chengdu 610225, China; uestc_hyjian@sina.com
* Correspondence: xiongp0808@sina.com

Abstract: In this study, a quenching experiment was conducted at atmospheric pressure to investigate the flow and heat-transfer characteristics of cylindrical rods made from SS, FeCrAl, and Zr-4 under various subcooling degrees (ΔT_{sub}). The inverse heat-conduction problem (IHCP) method and image-processing technique were utilized to determine the surface temperature and heat flux, vapor film thickness, and quench front propagation. The results show that smaller solid $k\rho c_p$ and larger ΔT_{sub} result in relatively more efficient quenching boiling heat transfer, thinner vapor film thickness, and greater quench front propagation velocity. The quench front originates at the bottom of the test specimen and becomes progressively larger in velocity with time. It eventually converges with the downward-propagating quench front in the upper middle of the test specimen. Moreover, at the beginning of quench front propagation, the SS and FeCrAl test specimens have a constant velocity region. However, because the Zr-4 test specimen has a small $k\rho c_p$, the velocities gradually increase from the onset of quench front generation. Furthermore, the measured average quench front velocities are consistent with the experimental datum from the literature. However, the predicted model proposed by Duffey underestimates the propagation velocity due to ignoring the cooling effect of film boiling.

Keywords: quenching; subcooled water; heat transfer; quench front; propagation velocity

check for updates

Citation: Sun, Y.; Jian, H.; Xiong, P.; Zhou, L. An Experimental Study of Boiling Heat Transfer and Quench Front Propagation Velocity During Quenching of a Cylinder Rod in Subcooled Water. *Energies* **2024**, *17*, 5236. https://doi.org/10.3390/en17205236

Academic Editors: Rajib Mahamud, John Boland, Ali Ashraf and Roxana Bujack

Received: 9 September 2024
Revised: 8 October 2024
Accepted: 17 October 2024
Published: 21 October 2024

Copyright: © 2024 by the authors. Licensee MDPI, Basel, Switzerland. This article is an open access article distributed under the terms and conditions of the Creative Commons Attribution (CC BY) license (https://creativecommons.org/licenses/by/4.0/).

1. Introduction

Quenching is a rapid cooling technique employed across various industrial applications [1,2], including heat treatment during steel manufacturing [3–5] and post-accident cooling of nuclear fuel following a loss of cooling accident (LOCA) [6,7]. During the initial stage of pressurized water reactor reflooding, film boiling manifests on the surface of fuel rods. As the surface temperature drops, the vapor film first breaks at the bottom of the fuel rods and travels upward, forming the quench front [3,8,9]. Upstream of the quench front, the fuel rods are enveloped by a vapor film with low thermal conductivity. Transition and nuclear boiling only occur downstream of the quench front on the surface of fuel rods, and the heat transfer efficiency is significantly improved [10]. Therefore, the quench front propagation velocity is a key parameter used to characterize the cooling efficiency of reactor reflooding during reflooding in a loss of cooling accident.

In recent decades, researchers have extensively investigated the boiling heat-transfer phenomenon during quenching. Early in the 1970s, Piggott et al. [11] conducted a quenching experiment on stainless steel and zirconium alloy tubes and found that the zirconium alloy tube cooled faster than the stainless steel tube. Fan et al. [12], Ebrahim et al. [13], Fu et al. [14], Dhir et al. [15], and Freud et al. [16] studied the quenching process of various metallic materials in deionized water at different subcooling degrees (ΔT_{sub}) and

constructed a relationship formula between the ΔT_{sub} and the minimum film boiling temperature (T_{min}). Li and Zhang et al. [17–19] used deposition and chemical-etching methods to prepare the surfaces with different surface wickability to investigate their impact on the quenching process. The experimental findings show that the etched specimens exhibited an absence of a stable film-boiling phase compared to unmodified surfaces, while the transitional boiling phase increased, and the critical heat flux (CHF) and T_{min} increased with a higher surface wickability capacity. Park and Lotfi et al. [20,21] studied the effects of nanofluids on quenching boiling, finding that compared to pure water, the film boiling heat flux and cooling rate of nanofluids are lower. Fan and Li et al. [12,22,23] studied the impact of surface wettability on quenching boiling, finding that improving surface wetness can enhance heat exchange efficiency during the quenching process. Particularly, superhydrophilic surfaces, with a nearly zero static contact angle, can significantly increase the quenching rate and the critical heat flux.

Numerous studies have been extensively investigated to reveal the influence of high-temperature materials, coolant types, and the coolant subcooling degree on the quench front propagation velocity. Ni et al. [24] studied the fluctuating velocity of the quench front on the surface of a heated sphere under the forced convection condition. The propagation of the quench front is influenced by the sphere temperature, liquid flow rate, and the coolant subcooling. Gupta et al. [25] conducted single-jet impingement quenching experiments using deionized water, Al_2O_3, and SiO_2 nanofluids, respectively. Compared to deionized water, the quench front propagation velocity of Al_2O_3 and SiO_2 nanofluids increased by 44% and 103%, respectively. Lee et al. [26] found that surface roughness had a negligible impact on the propagation velocity in rewetting experiments. Ohtake et al. [27] investigated the collapse of vapor film during film boiling on a highly superheated surface. The results show that the propagation velocity decreases with the drop in the localized cold spot temperature.

Scholars have established the empirical relationship of the quench front velocity based on experimental data and theoretical derivation. Murao et al. [28], Xu et al. [29], Piggott et al. [11,30], Yamanouchi et al. [31], and Duffey et al. [32] established empirical relations of the propagation velocity. By analyzing the heat conduction of the quenching surface, Duffey et al. [32] derived a theoretical solution of the propagation velocity, assuming that the heat transfer is zero in the film boiling region while considering it to be constant in the nucleate boiling phase. Piggott et al. [30] considered the impact of pressure and the coolant subcooling degree on the propagation velocity using reflooding experiments in narrow channels and derived the corresponding formula. Murao et al. [28] obtained an empirical relationship of the propagation velocity under flow experiment. The predictive accuracy of the relationship was within $\pm$20%, compared with the experimental values of Piggott et al. [30]. Xu et al. [29,33,34] studied the thermal characteristics of plate-type fuel elements in narrow rectangular channels and proposed an analytical model of quench front based on energy balance, which showed good consistency with experimental values.

In this work, quenching experiments were performed with different materials (SS, FeCrAl, and Zr-4) and the coolant subcooling degree. Utilizing the inverse heat-conduction problem (IHCP) method, this research sheds more light on the heat-transfer characteristics of quenching boiling. Furthermore, the image-processing technique, which involves processing visual images to determine the vapor film thickness, is employed to explore the boiling heat transfer modes and the vapor film fluctuation behavior during quenching. The variation of quench front propagation with the subcooling degree and material of the test specimen are analyzed based on the reconstructed full-scale transient 2-D vapor film image.

2. Experimental Apparatus and Test Specimen

Figure 1 illustrates the quenching experimental apparatus, which mainly consists of a radiant furnace to heat the test specimen, a stepping motor to move the hot test specimen, a quartz glass quenchant pool, and a data acquisition system to obtain visual and temperature acquisition. Detailed parameters of these devices are described in our previous work [35].

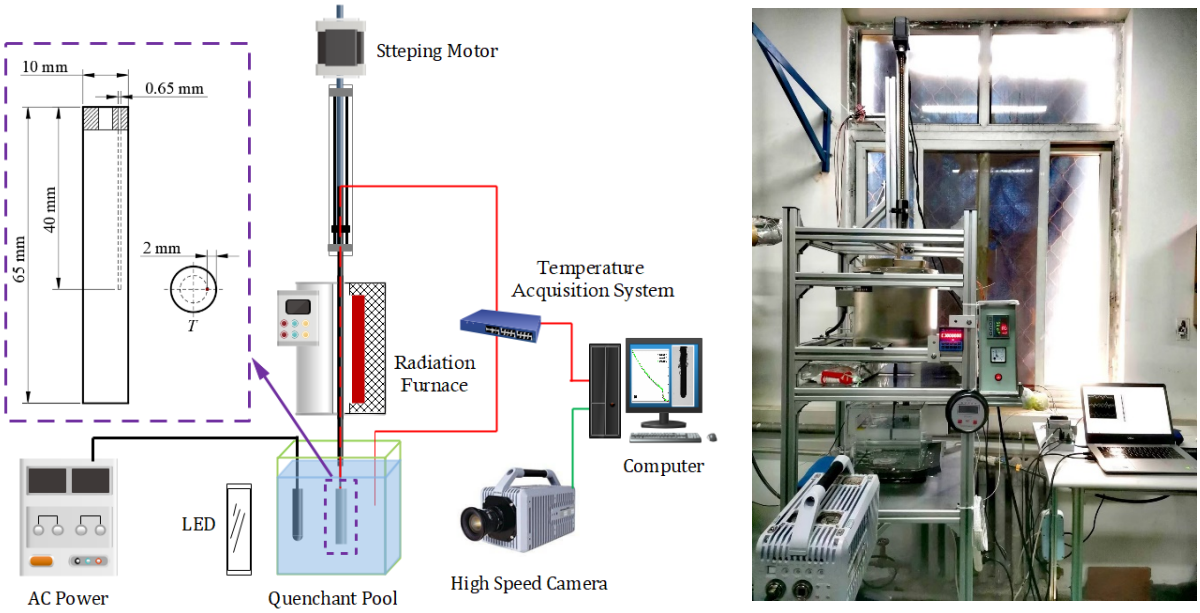

(**a**) Schematic diagram (**b**) Photograph

Figure 1. Experimental apparatus of quenching.

The test specimen, measuring 10 mm in diameter and 65 mm in length, is made of 316L stainless steel (SS), accident tolerant fuel (ATF) cladding materials (FeCrAl), or Zircaloy-4 (Zr-4) material. Table 1 displays the thermophysical properties of these materials. A micro-hole with a length of 40 mm and a diameter of 0.65 mm is arranged 2 mm away from the cylindrical surface for the installation of the thermocouple. The test specimens are sanded with sandpaper to achieve an average surface roughness of 0.2 micrometers. Prior to conducting the quenching experiment, the polished surfaces of the specimens are cleansed in a water bath using an ultrasonicator to eliminate any dust particles. The quenchant pool used in this study has dimensions of 250 mm × 200 mm × 200 mm, which is larger than the dimensions of the test specimen (diameter of 10 mm, length of 65 mm). During the boiling process, the test specimen is placed at the center of the quenchant pool, fully meeting the experimental requirements for the size of the quenchant pool [36].

Table 1. Material properties values of test specimen [37–39].

Material	Properties	Values
SS	Density	$\rho = 7900$ [kg/m^3]
	Specific heat capacity	$c_p = 467.081 + 0.253T - 7.317 \times 10^{-5}T^2$ [J/(kg·°C)]
	Thermal conductivity	$k = 12.877 + 2.575 \times 10^{-2}T - 1.045 \times 10^{-5}T^2$ [W/(m·°C)]
FeCrAl	Density	$\rho = 7250$ [kg/m^3]
	Specific heat capacity	$c_p(T) = 432.926 + 0.852T - 1.867 \times 10^{-3}T^2 + 2.982 \times 10^{-6}T^3$ [J/(kg·°C)]
	Thermal conductivity	$k(T) = 10.776 + 1.521 \times 10^{-2}T - 7.223 \times 10^{-7}T^2$ [W/(m·°C)]
Zr-4	Density	$\rho = 6550$ [kg/m^3]
	Specific heat capacity	$c_p(T) = 283.631 + 0.1024T$ [J/(kg·°C)]
	Thermal conductivity	$k(T) = 13.289 - 4.363 \times 10^{-3}T + 8.982 \times 10^{-6}T^2$ [W/(m·°C)]

Before the quenching experiments, 5 L of deionized water is heated to the target temperature using a Joule heating rod. The test specimen is positioned at the central location of the radiative heating furnace and heated to about 600 °C. When the temperatures of the specimen and water reach the desired points and remain stable, the specimen is plunged into the quenchant pool via the stepping motor, and the quenching is triggered.

The visualized boiling behavior and temperature variations are recorded using a high-speed camera and thermocouple, respectively. The acquisition frequency of the high-speed camera is set as 250 fps with a resolution of 1024 pixels × 1024 pixels. The acquisition frequency of the K-type thermocouple is set as 50 Hz. The quenching experiment ends when the experimental test specimen temperature falls below 100 °C. To achieve the best picture effect, it is essential to adjust both the intensity of incident light and exposure duration from the high-speed camera and add the LED light source as a supplement.

3. Data Reduction

In order to capture the morphology evolution of the vapor film, high-speed videos are used to measure the boiling behavior during the quenching process. In this study, an advanced image processing technique is used to reconstruct a full-scale transient 2-D vapor film image and obtain the quantitative parameters of quench front propagation. Figure 2 illustrates the calculation procedures of the reconstructed vapor film.

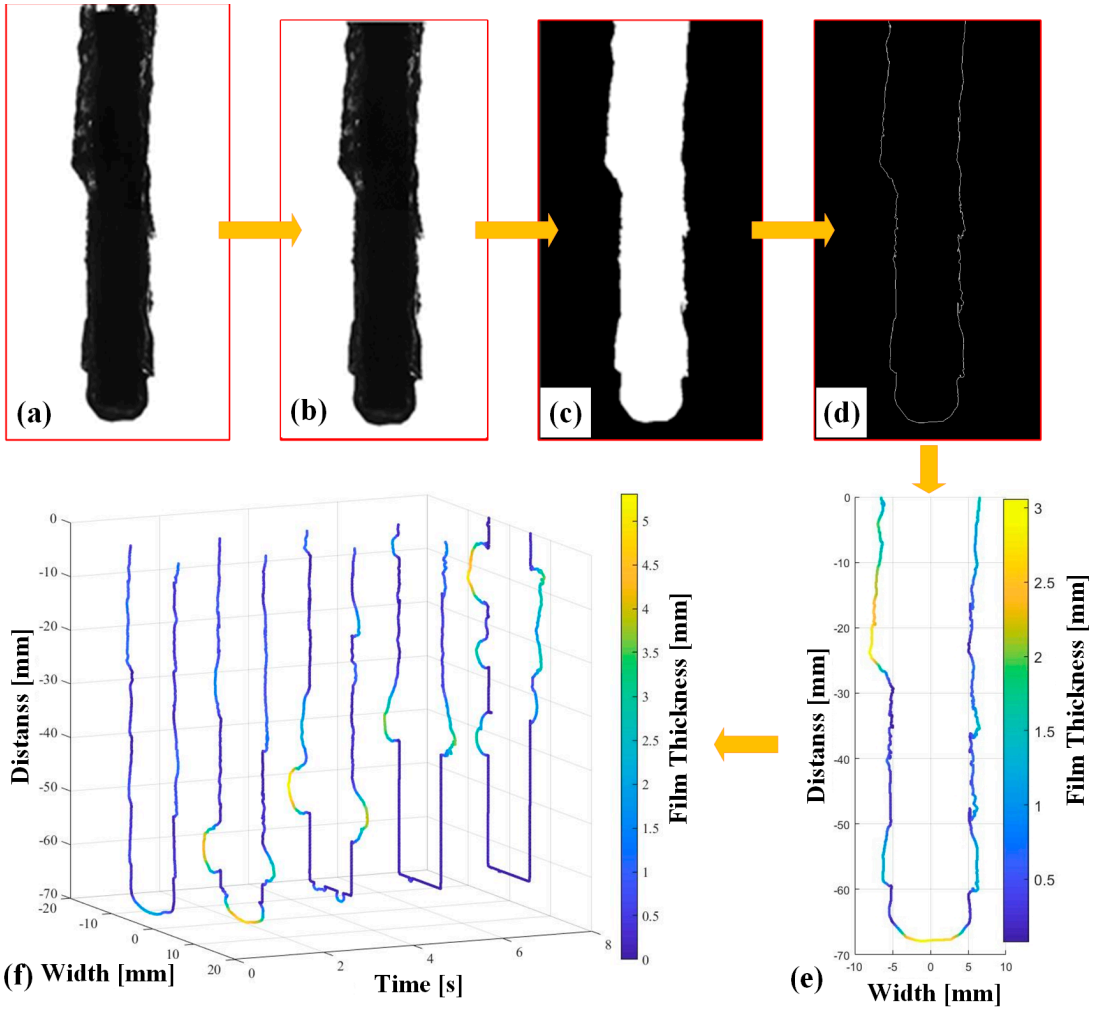

Figure 2. Procedures of reconstructed vapor film thickness. (**a**) Original image, (**b**) grayscale image, (**c**) binary images, (**d**) vapor–liquid interface, (**e**) film thickness, and (**f**) reconstructed 2-D topology vapor film.

(1) The original images to be processed are selected in sequence and imported into MATLAB 2016a software, as shown in Figure 2a.

(2) The selected original RGB color images need to be converted to grayscale images, and the cropping tool is used to crop to the region of interest, as illustrated in Figure 2b.

(3) Grayscale images are transformed into binary images using a thresholding tool with binary options. The value of the intensity threshold, depending on the brightness, degree of focus, and contrast of the shooting process, is set as 125 in this experiment. The final binary images are shown in Figure 2c. In this step, to more accurately detect the vapor–liquid interface, the small holes in the binary image will be filled.

(4) Then, the Laplacian Gaussian filter is used to detect and identify the edge of the processed binary image, as shown in Figure 2d—that is, the liquid–vapor interface of quenching boiling.

(5) According to the pixel size of the test specimen in the image, the pixel ratio can be obtained. The pixel ratio equals the diameter (10 mm) of the test specimen divided by the number of pixels. The pixel size of the vapor film for each frame image is determined by calculating the pixel difference between the detected edge of the vapor film and the test specimen. Finally, using the pixel ratio in the image, the vapor film thickness is determined by converting pixel distances to millimeter distances, as shown in Figure 2e. In the current setup, the measurement resolution of the video data is 0.075 mm per pixel. Therefore, the accuracy of the vapor film thickness obtained through the image-processing technique is $\pm$0.075 mm.

(6) Finally, the film thickness images identified in each frame are integrated for the quenching duration to generate the morphology evolution images. Consequently, a reconstructed 2-D topology vapor film that varies with time and the axial direction can be achieved, as shown in Figure 2f.

4. Results and Discussion

4.1. Boiling Heat-Transfer Characteristics

To avoid the influence of surface-mounted thermocouples on the quenching phenomenon, the thermocouples are positioned at a distance of 2 mm from the cylindrical surface. Subsequently, the surface temperature and heat flux can be determined using the IHCP method, as outlined in our previous work [40]. Figure 3 shows the quenching temperature curves and quenching boiling curves of three materials under different ΔT_{sub}.

The quenching temperature curve shifts leftward, and the duration of the quenching is reduced with the increase in ΔT_{sub}, as shown in Figure 3a. During the film-boiling phase, as the ΔT_{sub} increases, the absolute value of the slope of the quenching temperature curve gradually increases, indicating that as the temperature of subcooled water decreases, the film-boiling process is enhanced. As the quenching process continues, the absolute values of the slopes of the temperature curves for SS, FeCrAl, and Zr-4 further increase, entering the transition boiling phase until reaching the position of maximum absolute slope value. Afterward, the slope of the temperature curve gradually decreases as the quenching process enters the nucleate boiling phase. Figure 3b shows the corresponding boiling curve. With the increase in ΔT_{sub}, the boiling curve exhibits a noticeable shift toward the upper right corner. As ΔT_{sub} increases, heat transfer is enhanced during the film-boiling phase. This phenomenon primarily arises from the thinner vapor film thickness at higher ΔT_{sub}, and the heat conduction resistance of the vapor film is reduced. Therefore, its heat transfer capacity is somewhat enhanced. However, due to the inherently low thermal conductivity of the vapor film, its overall heat transfer capacity remains relatively low. Figure 4 illustrates the variation of the critical heat flux (CHF), temperature of the critical heat flux (T_{CHF}), and T_{min} with ΔT_{sub} during quenching. It can be seen that CHF, T_{CHF}, and T_{min} almost increase linearly with the increase in the coolant ΔT_{sub}. When ΔT_{sub} increases from 5 °C to 25 °C, the CHF, T_{CHF}, and T_{min} of the three materials nearly increase by approximately 1.2, 0.6, and 1 times, respectively.

Regarding the heat transfer performance of different materials, the quenching duration time of FeCrAl, SS, and Zr-4 materials decreases successively, as shown in Figure 3a. This is because the material thermophysical properties $k\rho c_p$ of FeCrAl, SS, and Zr-4 materials gradually decline. More energy will be released for FeCrAl material with larger $k\rho c_p$ at the same temperature gradient. Consequently, the FeCrAl sample exhibits a longest quenching

duration time. However, owing to the inherently low thermal conductivity resistance of the vapor film, the surface heat flux of film-boiling stage is almost the same for all three materials.

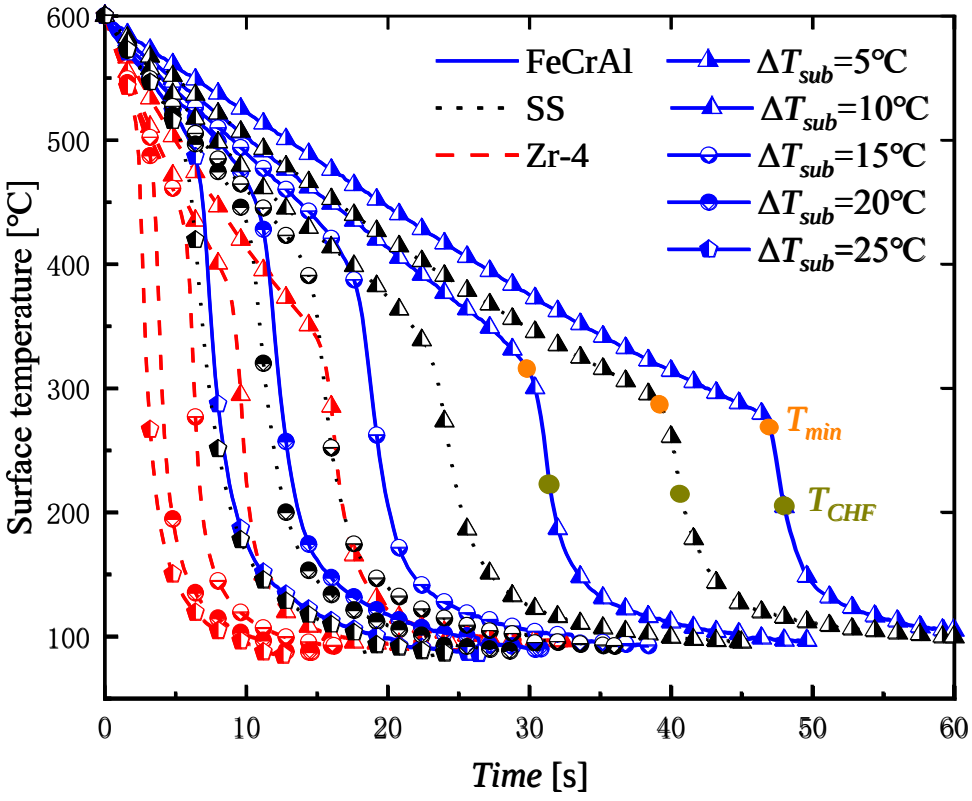

(**a**) Quenching temperature curve

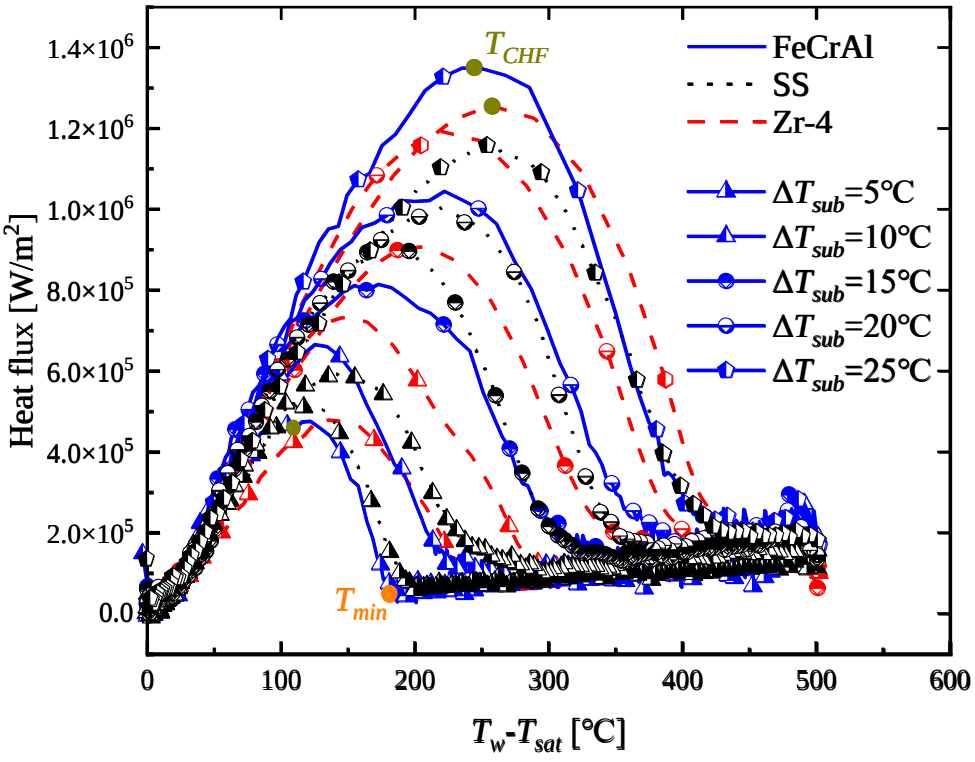

(**b**) Boiling curve

Figure 3. Quenching temperature curve and boiling curve under different ΔT_{sub}.

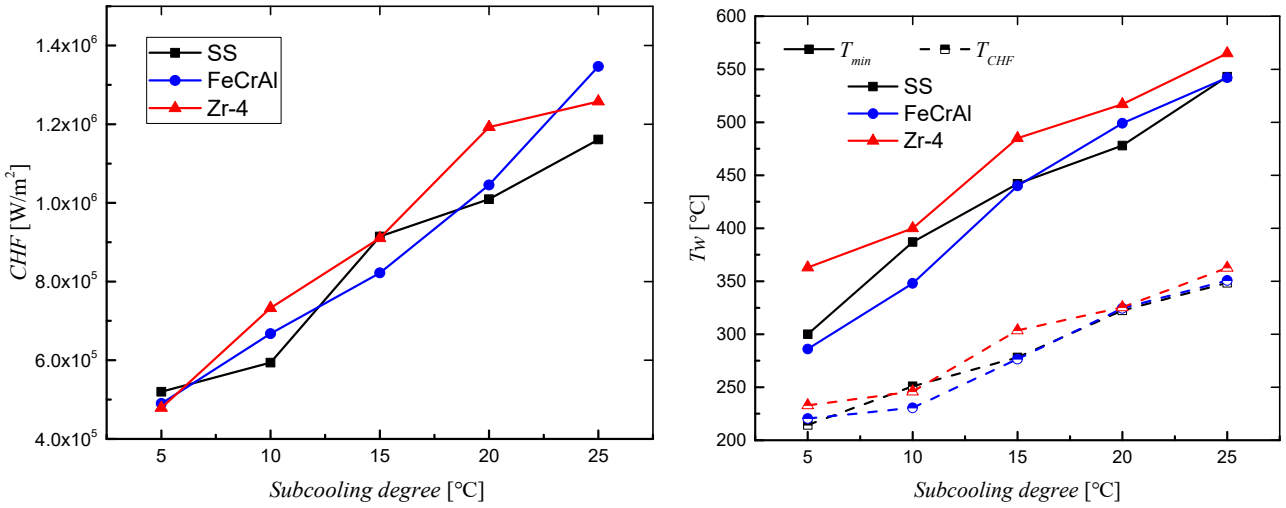

(**a**) CHF (**b**) T_{CHF} and T_{min}

Figure 4. Variation in critical heat flux (CHF), temperature of critical heat flux (T_{CHF}), and T_{min} with ΔT_{sub} during quenching.

4.2. Visualization Results

Figures 5–7 depict the quenching boiling visualization for SS, FeCrAl, and Zr-4 specimens at different ΔT_{sub}, respectively. During the film-boiling stage, under low ΔT_{sub} conditions (ΔT_{sub} = 5 °C), the vapor film is thicker, and the Kelvin–Helmholtz instability wave fluctuations is larger. As the coolant ΔT_{sub} increases, the vapor produced on the surface condenses rapidly, resulting in a reduction in vapor film thickness. Moreover, higher ΔT_{sub} also leads to the shortening of the film's boiling duration. This is because a thinner vapor film accelerates the collapse of the vapor film. The surface vapor film motion states of the three materials are identical during the film-boiling phase. However, the duration of film boiling and the time for generating vapor bubbles for FeCrAl, SS, and Zr-4 test specimens decrease sequentially. This is because the ρkc_p value of the three materials decreases progressively. The experience temperature of materials with a smaller ρkc_p value changes more rapidly, resulting in faster surface cooling rates. As time proceeds, the vapor film of film boiling collapses, and rewetting starts at the bottom of the test specimen, forming a quench front, which moves up along the wall of the test specimen with an apparent velocity, as indicated by the red arrows in Figures 5–7. Under low ΔT_{sub}, the vapor bubbles formed in the nucleate boiling zone are larger and propagate upwards under the action of buoyancy, causing disturbances to the vapor film of the upper film-boiling stage. However, due to the rapid condensation under the high subcooling, the disturbance to the film boiling area on the upper location of quench front is reduced.

4.3. Quench Front Propagation

To investigate the morphology of the vapor film and analyze the propagation velocity of the quench front during quenching, the advanced image-processing technique is employed to reconstruct the full-scale transient 2-D vapor film. Figures 8–10 show 3-D contour plots of the vapor film thickness for SS, FeCrAl, and Zr-4 materials under various coolant ΔT_{sub}, respectively. The red arrow line is used to highlight the path of the quench front. The observation reveals that the quench front initially emerges from the bottom of the specimen and subsequently expands upward. After propagating to a certain distance, a downward-propagating quench front appears at the upper end of the specimen. Finally, the upward-propagating quench front and downward-propagating quench front converge in the middle-upper position. With the increase in coolant ΔT_{sub}, the merging position of the upward-propagating and downward-propagating quench fronts moves closer to the upper end of the specimen.

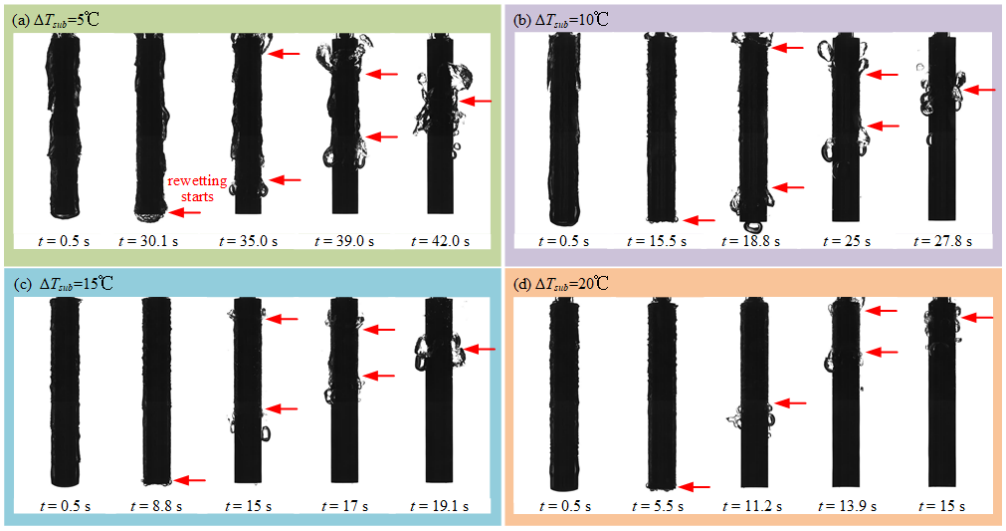

Figure 5. Evolution process of quench front of SS under different ΔT_{sub}.

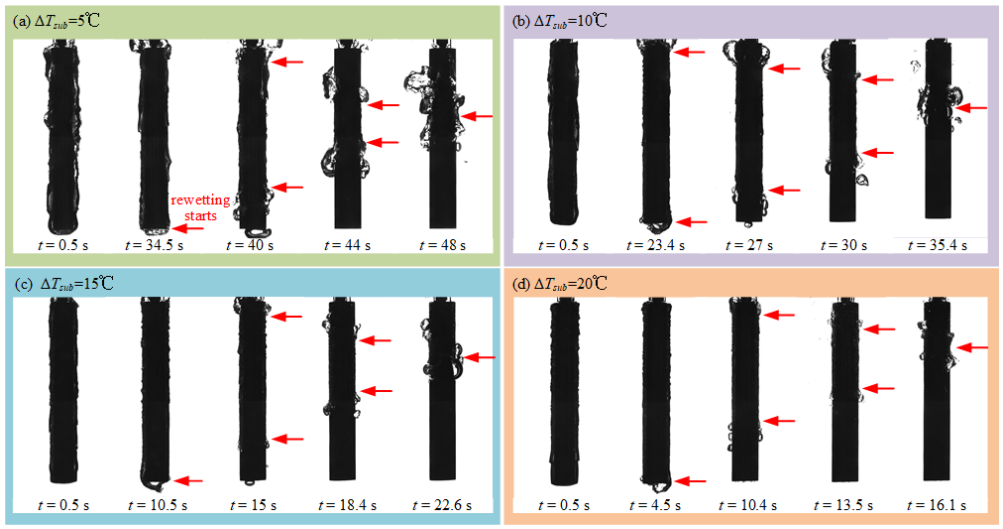

Figure 6. Evolution process of quench front of FeCrAl under different ΔT_{sub}.

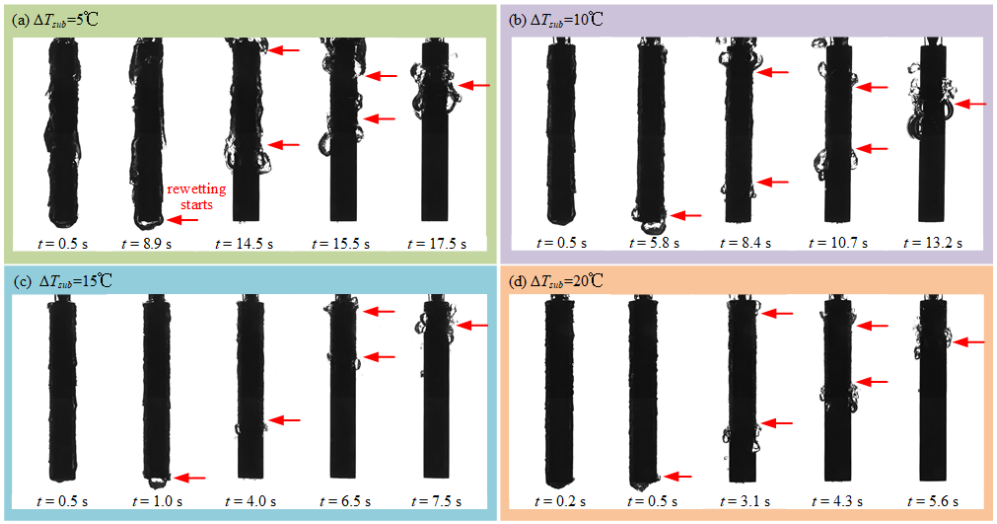

Figure 7. Evolution process of quench front of Zr-4 under different ΔT_{sub}.

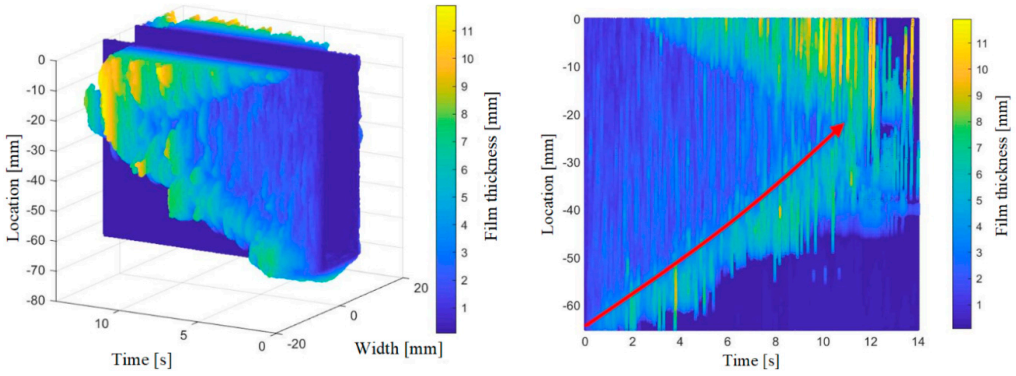

(**a**) ΔT_{sub} = 5 °C

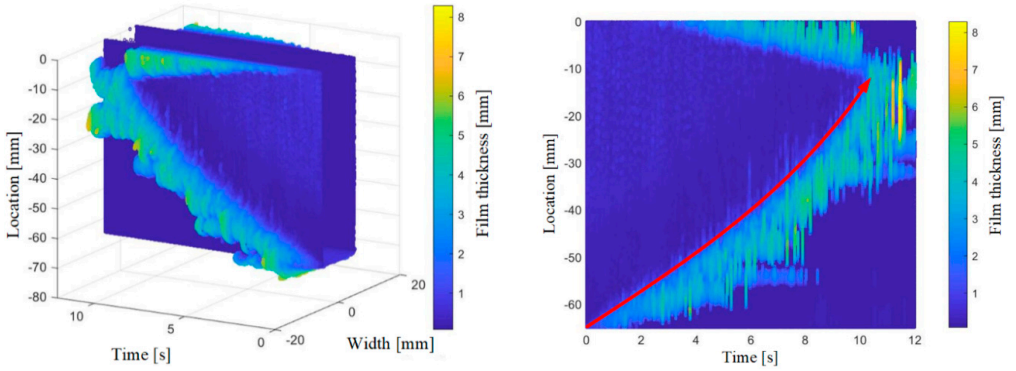

(**b**) ΔT_{sub} = 15 °C

Figure 8. Vapor film thickness of transition and nucleate boiling on SS surface under different ΔT_{sub}.

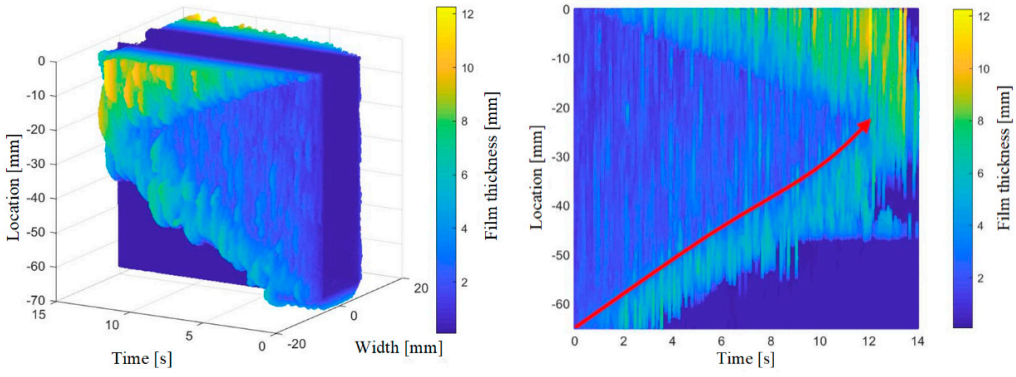

(**a**) ΔT_{sub} = 5 °C

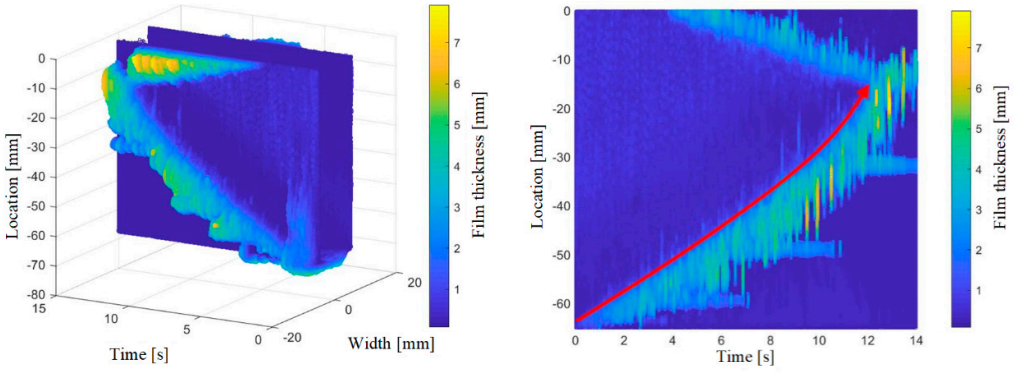

(**b**) ΔT_{sub} = 15 °C

Figure 9. Vapor film thickness of transition and nucleate boiling on FeCrAl surface under different ΔT_{sub}.

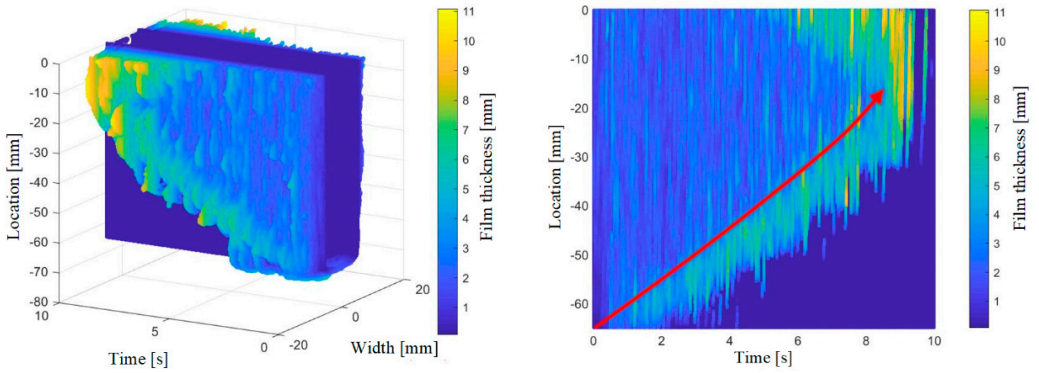

(**a**) ΔT_{sub} = 5 °C

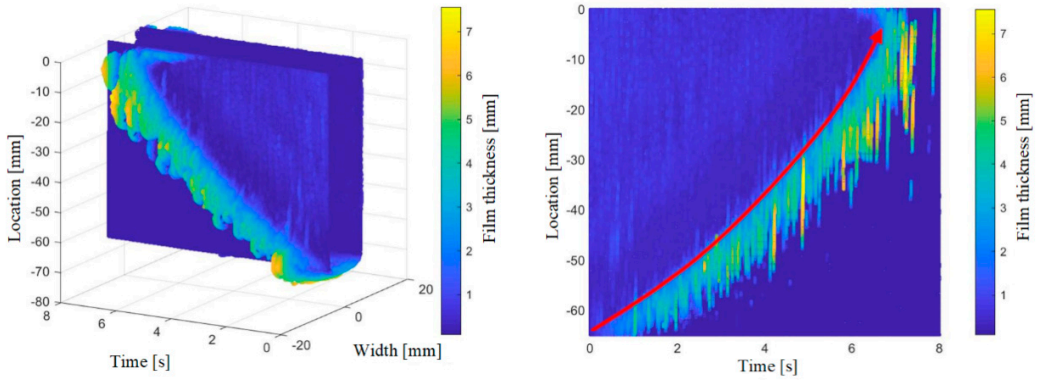

(**b**) ΔT_{sub} = 15 °C

Figure 10. Vapor film thickness of transition and nucleate boiling on Zr-4 surface under different ΔT_{sub}.

Figure 11 illustrates the temporal variation of the upward-propagating quench front position in the test specimen of the three materials under different ΔT_{sub}. Under low ΔT_{sub}, the quench front position varies approximately linearly with time. Conversely, under high ΔT_{sub}, the quench front position follows an upward parabolic trend over time, indicating a gradual acceleration of the propagation velocity. In addition, by comparing the changes of the quench front position under different ΔT_{sub}, the slope of the quench front curve increases with the increase in ΔT_{sub}, suggesting that a higher ΔT_{sub}, corresponds to a more rapid change in propagation velocity.

To quantitatively analyze the variation of the propagation velocity with the axial location and quenching time for the three materials, the partial derivatives of the quench front position with respect to time for each material in Figure 11 are calculated. The results are shown in Figures 12–14. The propagation velocity accelerates with the increase in ΔT_{sub}. Under low coolant ΔT_{sub}, the quench front of the SS, FeCrAl, and Zr-4 test specimen gradually propagated upwards from the bottom at velocities of 3.4 mm/s, 3.0 mm/s, and 4.4 mm/s. Finally, it converged with the upper quench front at velocities of 4.3 mm/s, 4.0 mm/s, and 6.8 mm/s, with a relatively gradual rate of increase. In comparison, under high coolant ΔT_{sub}, the quench front propagation velocity significantly increases. This is because under high ΔT_{sub}, the vapor film thickness in film boiling is thinner, causing the precursor cooling effect (the cooling effect of the film boiling regime upstream of the quench front position) to become more pronounced. In addition, the T_{min} used to maintain stable film boiling increases under high ΔT_{sub}, which is conducive to the upward propagation of the quench front region. When the coolant ΔT_{sub} is 25 °C, for SS, FeCrAl, and Zr-4 test specimens, the quench front propagation velocity increases from the initial 4.4 mm/s, 3.7 mm/s, and 6.8 mm/s to the final 12.3 mm/s, 8.1 mm/s, and 22.5 mm/s, showing an approximate 2–3 times increase.

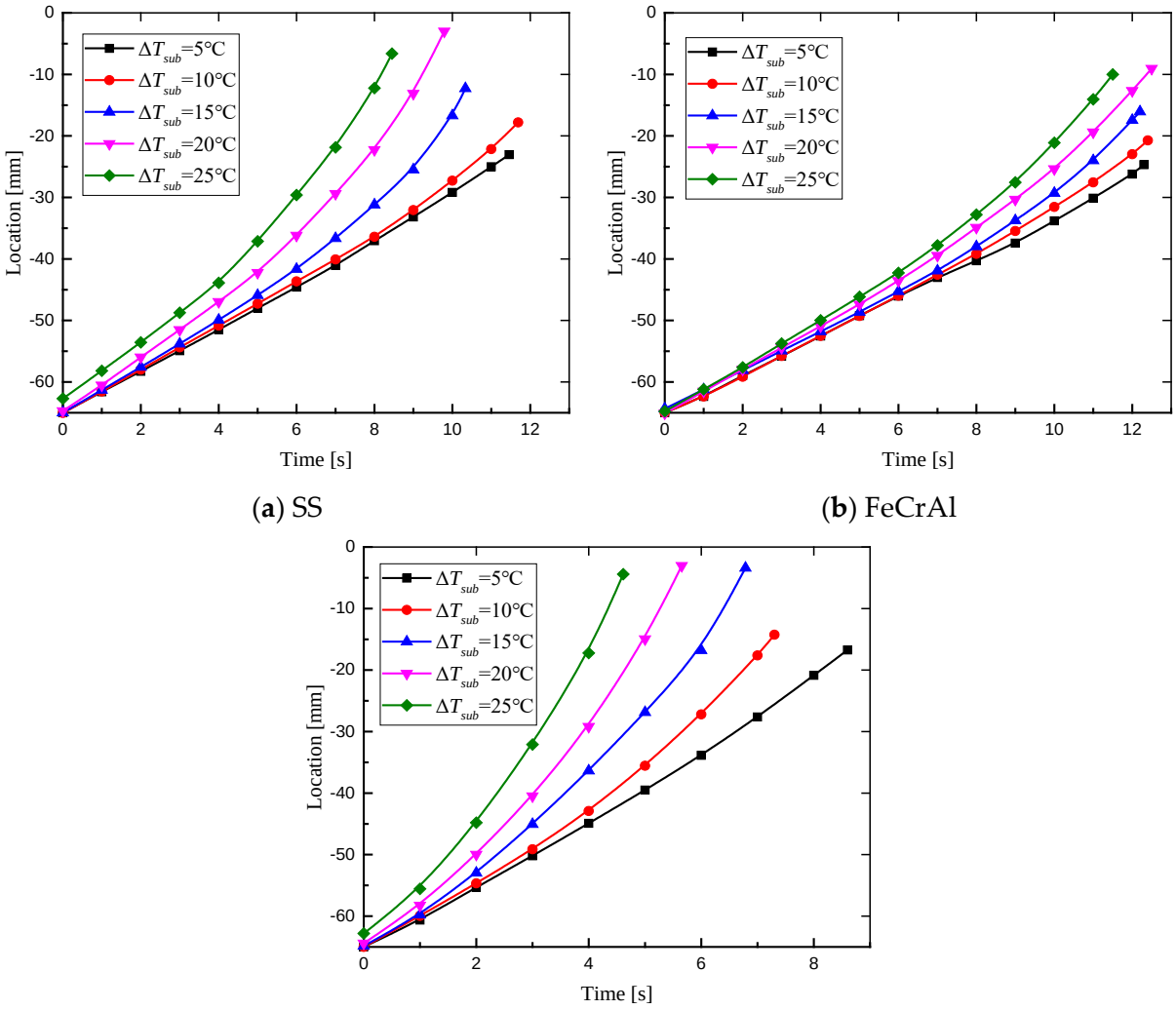

Figure 11. Change of quench front position with time.

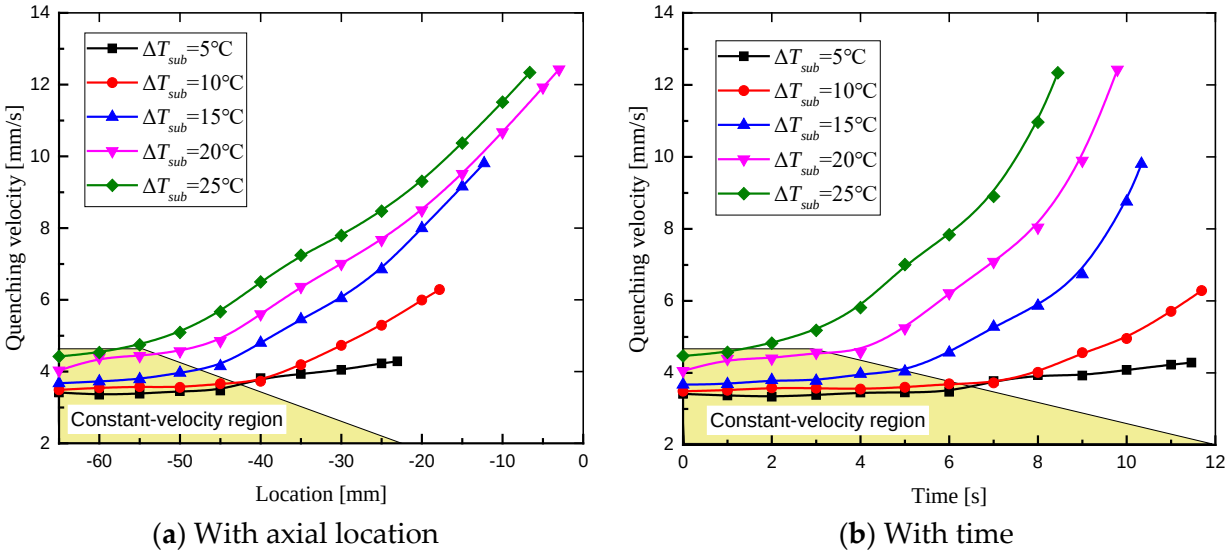

Figure 12. Quench front propagation velocity of SS surface under different ΔT_{sub}.

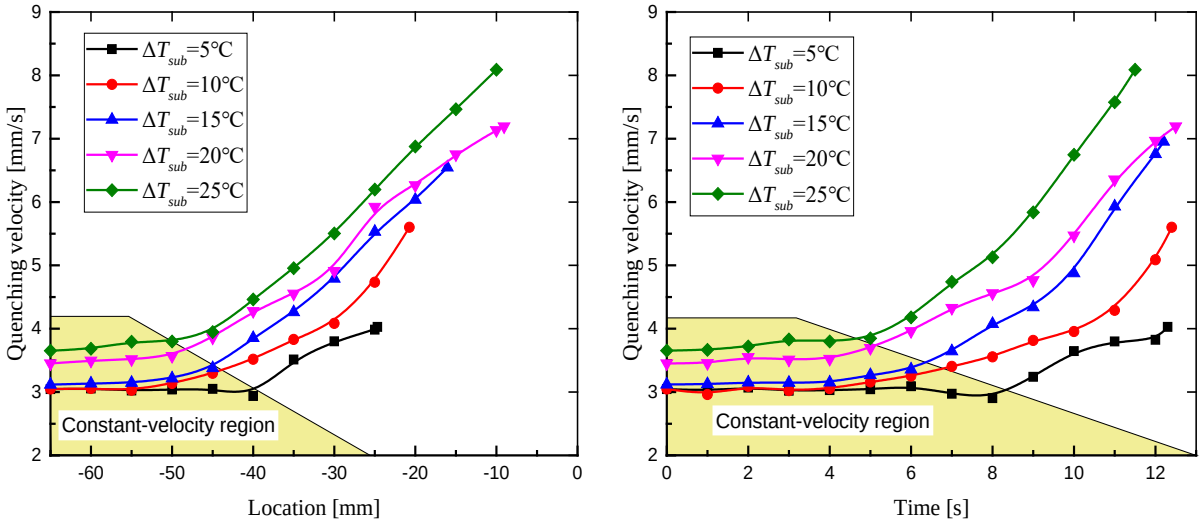

(**a**) With axial location (**b**) With time

Figure 13. Quench front propagation velocity of FeCrAl surface under different ΔT_{sub}.

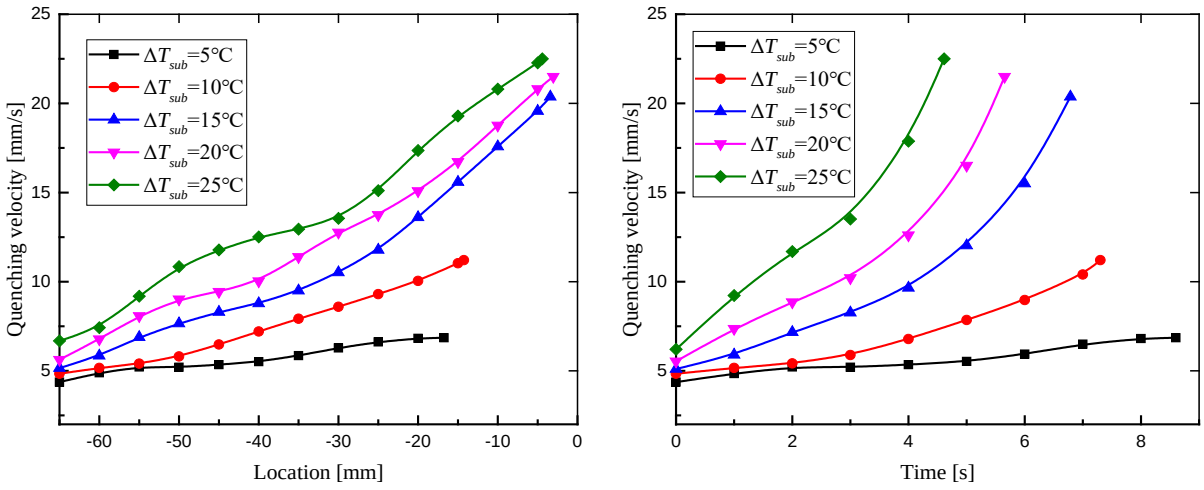

(**a**) With axial location (**b**) With time

Figure 14. Quench front propagation velocity of Zr-4 surface under different ΔT_{sub}.

For the SS and FeCrAl test specimen, there is a constant velocity region for the propagation velocity at the beginning of the propagation. This is primarily because the surface temperature of the rod is relatively high, and the precursor cooling effect is weak, which inhibits the rapid growth of the propagation velocity. Only when the quench front propagates upward to a certain position does the propagation velocity increase significantly. Additionally, it can be observed that as ΔT_{sub} increases, the constant velocity region progressively shortens. However, there is no constant velocity region in the Zr-4 test specimen, and the quench front gradually increases from the beginning of its generation. This is because compared with SS and FeCrAl materials, Zr-4 material has smaller $k\rho c_p$, the total energy contained in the cylinder is smaller, and the surface temperature is more easily reduced.

4.4. Analyzing Quench Front Propagation: Experimental Data vs. Duffey's Model

The prediction of the propagation velocity holds significant importance in elucidating the underlying principles governing flow behavior and heat transfer performance during quenching. Duffey and Porthouse [32] analyzed surface heat transfer in a high-temperature test specimen and obtained a theoretical solution for the quench front propagation velocity based on two-dimensional analysis.

$$u = \frac{2h(T_{min} - T_l)}{\pi \rho_w c_{p,w}(T_{ini} - T_l)} \left[1 - \frac{4}{\pi^2} Bi \frac{(T_{min} - T_l)}{(T_{ini} - T_l)}\right]^{-0.5} \quad (1)$$

where Bi is the Biot number, which is equal to hR/k_w. ρ_w and $c_{p,w}$ represent the density and specific heat capacity of the test specimen. T_{ini} and T_l represent the initial heated surface temperature and the coolant temperature, respectively. h represents the heat transfer coefficient in the wetted area. Piggott and Porthouse [11] conducted theoretical analysis and proposed that the heat transfer coefficient of the boiling surface is related to the heated surface temperature. They derived the heat transfer coefficient for the quench front phase as follows.

$$h = \frac{\int_{T_{sat}}^{T_{min}} q(T)dT}{\int_{T_{sat}}^{T_{min}} (T - T_{sat})dT} \quad (2)$$

As depicted in Figures 12–14, when the quench front propagates in the upper part of the test specimen, its propagation velocity exhibits a significant increase. Hence, the average velocity of lower part of test specimen below 20 mm is used to represent the measured average propagation velocity. Figure 15 presents a comparison of the average propagation velocity at different ΔT_{sub} for three materials using Duffey's correlation and the experimental data. Compared with SS and FeCrAl materials, the average propagation velocity of Zr-4 material is higher. This is because Zr-4 material has smaller thermophysical properties parameters ($k\rho c_p$), which leads to a faster cooling rate on the downstream surface of the quench front and accelerates the rewetting process. Li et al. [23], Kim et al. [41], and Kang et al. [42] studied quenching heat transfer and the propagation velocity on the surface of a vertical cylinders and obtained the average propagation velocity. As depicted in Figure 15, the experimental values of the propagation velocity demonstrate a close alignment with the literature data.

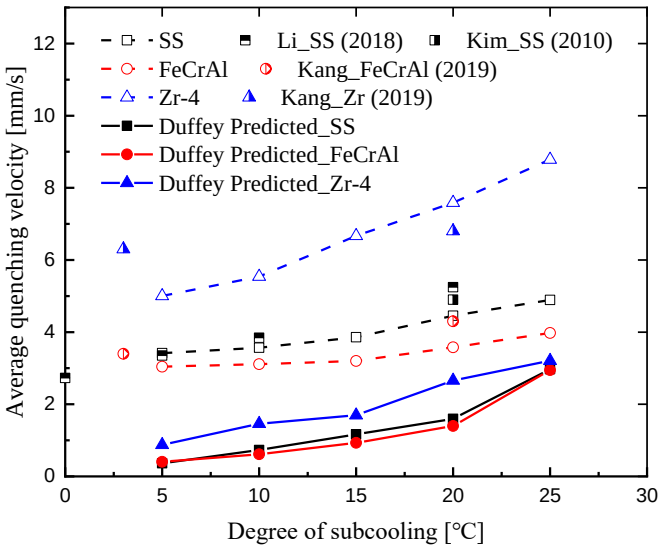

Figure 15. Comparisons of predicted average quench front propagation velocity of Duffey's correlation and experimental value [23,41,42].

Compared with the experimental data, Duffey's correlation underestimates the propagation velocity. This discrepancy primarily arises because Duffey's correlation ignores the cooling effect of film boiling on the upstream of the quench front and simplifies it to the adiabatic surface, resulting in the predicted propagation velocity being lower than the experimental value. In addition, T_{min}, the predicted propagation velocity, is affected by various parameters, including thermophysical properties, surface morphology, ΔT_{sub}, and so on [43–45]. For different experimental conditions, there may be some differences in the measurement of T_{min}, which leads to a difference in the predicted propagation velocity.

5. Conclusions

This study involves an experimental analysis of boiling heat transfer and quench front propagation velocity of SS, FeCrAl, and Zr-4 test specimens under different coolant subcooling during quenching. To ascertain the surface temperature and heat flux of the test specimen, the IHCP method was utilized. Using advanced image-processing technology, a full-scale transient 2-D steam film reconstruction is performed, and the propagation of the quench front is captured. Based on precedent in the Section 4, the principal findings are as follows,

(1) The increase in the coolant subcooling degree notably improves the heat transfer efficiency. When the coolant subcooling ΔT_{sub} increases from 5 °C to 25 °C, the T_{min} and critical heat flux increase significantly, corresponding to an increase of nearly 1 times and 1.2 times, respectively.

(2) Based on the visualization results, with increasing coolant subcooling, the vapor film thickness becomes thinner, and the oscillations gradually weaken. The quench front first originates at the bottom of the test specimen, propagates upward with increasing velocity over time, and finally converges with the downward-propagating quench front in the upper middle of the test specimen.

(3) As the coolant subcooling degree increases, the quench front propagation velocity accelerates noticeably. Due to the relatively weak precursor cooling effect, the SS and FeCrAl test specimens with higher $k\rho c_p$ exhibit a constant velocity region during the initial propagation of the quench front. In contrast, zirconium-4 alloy, which has a lower $k\rho c_p$, shows a higher propagation velocity.

(4) The measured average quench front velocities are consistent with the experimental datum from Li, Kim, and Kang. However, the predicted model proposed by Duffey underestimates the propagation velocity, primarily due to ignoring the cooling effect of film boiling.

Author Contributions: Validation, Y.S., H.J. and P.X.; Investigation, Y.S., P.X. and L.Z.; Data curation, H.J.; Writing—original draft, Y.S.; Writing—review & editing, H.J. and P.X.; Visualization, Y.S. and L.Z.; Funding acquisition, P.X. All authors have read and agreed to the published version of the manuscript.

Funding: This work is financially supported by the National Natural Science Foundation of China (No. 52206116).

Data Availability Statement: The original contributions presented in the study are included in the article, further inquiries can be directed to the corresponding author.

Conflicts of Interest: The authors declare no conflict of interest.

References

1. Lu, J.F.; Bourouga, B.; Ding, J. Transient boiling heat transfer performances of subcooled water during quenching process. *Int. Commun. Heat Mass Transf.* **2013**, *48*, 15–21. [CrossRef]
2. Starodubtseva, I.P.; Pavlenko, A.N.; Surtaev, A.S. Heat transfer during quenching of high temperature surface by the falling cryogenic liquid film. *Int. J. Therm. Sci.* **2017**, *114*, 196–204. [CrossRef]
3. Stepanek, J.; Blaha, V.; Dostal, V.; Entler, S. Effective water cooling of very hot surfaces during the LOCA accident. *Fusion Eng. Des.* **2017**, *124*, 1211–1214. [CrossRef]
4. Totten, G.E. *Steel Heat Treatment Metallurgy and Technologies*; Taylor and Francis Group: Boca Raton, FL, USA, 2006; pp. 540–545.
5. Li, J.Q.; Mou, L.W.; Zhang, Y.H.; Yu, J.Q.; Fan, L.W.; Yu, Z.T. Pool boiling heat transfer and quench front velocity during quenching of a rodlet in subcooled water: Effects of the degree of subcooling. *Exp. Heat Transf.* **2018**, *31*, 148–160. [CrossRef]
6. Pettersson, K.; Billone, M.; Fuketa, T.; Grandjean, C.; Zimmermann, M. *Nuclear Fuel Behaviour in Loss-of-Coolant Accident (LOCA) Conditions State-of-the-Art Report*; Nuclear Energy Agency (NEA): Paris, France, 2009.
7. Hwang, G.S.; In, W.K.; Lee, C.Y. Quenching experiments of vertical inconel and zircaloy tubes in internal water flow. *Ann. Nucl. Energy* **2022**, *167*, 108798. [CrossRef]
8. Wang, Z.F.; Zhong, M.J.; Deng, J.; Liu, Y.; Huang, H.J.; Zhang, Y.; Xiong, J.B. Experimental investigation on the transient film boiling heat transfer during quenching of FeCrAl. *Ann. Nucl. Energy* **2021**, *150*, 107842. [CrossRef]
9. Xiong, J.B.; Wang, Z.F.; Xiong, P.; Lu, T.; Yang, Y.H. Experimental investigation on transient boiling heat transfer during quenching of fuel cladding surfaces. *Int. J. Heat Mass Transf.* **2020**, *148*, 119131. [CrossRef]

10. Starodubtseva, I.P.; Kuznetsov, D.V.; Pavlenko, A.N. Experiments and modeling on cryogenic quenching enhancement by the structured capillary-porous coatings of surface. *Int. J. Heat Mass Transf.* **2021**, *176*, 121388. [CrossRef]
11. Piggott, B.D.G.; Duffey, R.B. The quenching of irradiated fuel pins. *Nucl. Eng. Des.* **1975**, *32*, 182–190. [CrossRef]
12. Fan, L.W.; Li, J.Q.; Su, Y.Y.; Wang, H.L.; Ji, T.; Yu, Z.T. Subcooled pool film boiling heat transfer from spheres with superhydrophobic surfaces: An experimental study. *J. Heat Transf.* **2016**, *138*, 021503. [CrossRef]
13. Ebrahim, S.A.; Chang, S.; Cheung, F.B.; Bajorek, S.M. Parametric investigation of film boiling heat transfer on the quenching of vertical rods in water pool. *Appl. Therm. Eng.* **2018**, *140*, 139–146. [CrossRef]
14. Fu, B.R.; Ho, Y.H.; Ho, M.X.; Pan, C. Quenching characteristics of a continuously-heated rod in natural sea water. *Int. J. Heat Mass Transf.* **2016**, *95*, 206–213. [CrossRef]
15. Dhir, V.K.; Purohit, G.P. Subcooled film-boiling heat transfer from spheres. *Nucl. Eng. Des.* **1978**, *47*, 49–66. [CrossRef]
16. Freud, R.; Harari, R.; Sher, E. Collapsing criteria for vapor film around solid spheres as a fundamental stage leading to vapor explosion. *Nucl. Eng. Des.* **2009**, *239*, 722–727. [CrossRef]
17. Zhang, J.Y.; Fan, L.W.; Li, J.Q.; Yu, Z.T. Surface-roughness-boosted critical heat flux enhancement during quenching boiling on wicking surfaces. *Int. J. Heat Mass Transf.* **2020**, *162*, 120364. [CrossRef]
18. Li, J.Q.; Mou, L.W.; Zhang, J.Y.; Zhang, Y.H.; Fan, L.W. Enhanced pool boiling heat transfer during quenching of water on superhydrophilic porous surfaces: Effects of the surface wickability. *Int. J. Heat Mass Transf.* **2018**, *125*, 494–505. [CrossRef]
19. Li, J.Q.; Zhang, J.Y.; Mou, L.W.; Zhang, Y.H.; Fan, L.W. Enhanced transitional heat flux by wicking during transition boiling on microporous hydrophilic and superhydrophilic surfaces. *Int. J. Heat Mass Transf.* **2019**, *141*, 835–844. [CrossRef]
20. Lotfi, H.; Shafii, M.B. Boiling heat transfer on a high temperature silver sphere in nanofluid. *Int. J. Therm. Sci.* **2009**, *48*, 2215–2220. [CrossRef]
21. Park, H.S.; Shiferaw, D.; Sehgal, B.R.; Kim, D.K.; Muhammed, M. Film boiling heat transfer on a high temperature sphere in nanofluid. In Proceedings of the ASME 2004 Heat Transfer/Fluids Engineering Summer Conference, Charlotte, NC, USA, 11–15 July 2004; Volume 4, pp. 469–476.
22. Fan, L.W.; Li, J.Q.; Li, D.Y.; Zhang, L.; Yu, Z.T. Regulated transient pool boiling of water during quenching on nanostructured surfaces with modified wettability from superhydrophilic to superhydrophobic. *Int. J. Heat Mass Transf.* **2014**, *76*, 81–89. [CrossRef]
23. Li, J.Q.; Mou, L.W.; Zhang, Y.H.; Yang, Z.S.; Hou, M.H.; Fan, L.W.; Yu, Z.T. An experimental study of the accelerated quenching rate and enhanced pool boiling heat transfer on rodlets with a superhydrophilic surface in subcooled water. *Exp. Therm. Fluid Sci.* **2018**, *92*, 103–112. [CrossRef]
24. Ni, P.; Wen, Z.; Su, F.Y.; Liu, X.L.; Lou, G.F. Breaking process of boiling film around a solid hot sphere immersed in forced convection of sub-cooled water. *Int. J. Heat Mass Transf.* **2020**, *158*, 120064. [CrossRef]
25. Gupta, V.; Ghosh, P. Visualization of quench front propagation on heated rod through single jet impingement. *J. Heat Transf.-Trans. ASME* **2020**, *142*, 092301. [CrossRef]
26. Lee, Y.; Shen, W.Q. Effect of surface roughness on the rewetting process. *Int. J. Multiph. Flow* **1987**, *13*, 857–861. [CrossRef]
27. Ohtake, H.; Koizumi, Y. Study on propagative collapse of a vapor film in film boiling. *Int. J. Heat Mass Transf.* **2004**, *47*, 1965–1977. [CrossRef]
28. Murao, Y. Correlation of quench phenomena for bottom flooding during loss-of-coolant accidents. *J. Nucl. Sci. Technol.* **1978**, *15*, 875–885. [CrossRef]
29. Xu, W.; Guo, J.Y.; Liu, X.J.; Xiong, J.B.; Chai, X.; Zhang, T.F.; Cheng, X.; Zeng, W. Predictions of quench temperature and quench velocity in narrow rectangular channel of novel plate-type reactor. *Ann. Nucl. Energy* **2019**, *131*, 148–155. [CrossRef]
30. Piggott, B.D.G.; Porthouse, D.T.C. A correlation of rewetting data. *Nucl. Eng. Des.* **1975**, *32*, 171–181. [CrossRef]
31. Yamanouchi, A. Effect of core spray cooling in transient state after loss of coolant accident. *J. Nucl. Sci. Technol.* **1968**, *5*, 547–558. [CrossRef]
32. Duffey, R.B.; Porthouse, D.T.C. The physics of rewetting in water reactor emergency core cooling. *Nucl. Eng. Des.* **1973**, *25*, 379–394. [CrossRef]
33. Xu, W.; Xia, J.H.; Liu, X.J.; Liu, X.J.; Cheng, X.; Zeng, W. Experimental investigation of bottom reflooding and modeling of quench velocity in a narrow rectangular channel. *Prog. Nucl. Energy* **2018**, *105*, 21–28. [CrossRef]
34. Xu, W.; Xia, J.H.; Liu, X.J.; Cheng, X.; Zeng, W. Study of bottom reflooding in a narrow rectangular channel. *Nucl. Technol.* **2019**, *205*, 281–296. [CrossRef]
35. Xiong, P.; Lu, T.; Luo, Y.; Zhang, Q.Q.; Ren, H.T.; Deng, J.; Heng, Y.G. Study on liquid-vapor interface oscillation characteristics and heat transfer of film boiling during quenching of fuel cladding surfaces. *Appl. Therm. Eng.* **2023**, *219*, 119615. [CrossRef]
36. Westwater, J.W.; Hwalek, J.J.; Irving, M.E. Suggested standard method for obtaining boiling curves by quenching. *Ind. Eng. Chem. Fundam.* **1986**, *25*, 685–692. [CrossRef]
37. Mills, K.C.; Su, Y.C.; Li, Z.S.; Brooks, R.F. Equations for the calculation of the thermophysical properties of stainless steel. *ISIJ Int.* **2004**, *44*, 1661–1668. [CrossRef]
38. Field, K.G.; Snead, M.A.; Yamamoto, Y.; Terrani, K.A. Handbook of the Materials Properties of FeCrAl Alloys for Nuclear Power Production Applications. 2018. Available online: https://info.ornl.gov/sites/publications/Files/Pub74128.pdf (accessed on 21 July 2024).
39. IAEA. *Thermophysical Properties Database of Materials for Light Water Reactors and Heavy Water Reactors*; IAEA: Vienna, Austria, 2006.

40. Xiong, P.; Deng, J.; Lu, T.; Lu, Q.; Liu, Y.; Zhang, Y. A sequential conjugate gradient method to estimate heat flux for nonlinear inverse heat conduction problem. *Ann. Nucl. Energy* **2020**, *149*, 107798. [CrossRef]
41. Kim, H.; Buongiorno, J.; Hu, L.W.; Mckrell, T. Nanoparticle deposition effects on the minimum heat flux point and quench front speed during quenching in water-based alumina nanofluids. *Int. J. Heat Mass Transf.* **2010**, *53*, 1542–1553. [CrossRef]
42. Kang, J.Y.; Kim, T.K.; Lee, G.C.; Jo, H.; Kim, M.H.; Park, H.S. Impact of system parameters on quenching heat transfer in the candidate materials for accident tolerant fuel-cladding in LWRs. *Ann. Nucl. Energy* **2019**, *129*, 375–389. [CrossRef]
43. Peterson, L.J.; Bajorek, S.M. Experimental investigation of minimum film boiling temperature for vertical cylinders at Elevated Pressure. In Proceedings of the 10th International Conference on Nuclear Engineering, Arlington, VA, USA, 14–18 April 2002; pp. 883–892.
44. Sinha, J.; Hochreiter, L.E.; Cheung, F.B. Effects of surface roughness, oxidation level, and liquid subcooling on the minimum film boiling temperature. *Exp. Heat Transf.* **2003**, *16*, 45–60. [CrossRef]
45. Adler, M.R. The Influence of Water Purity and Subcooling on the Minimum film Boiling Temperature. Master's Thesis, University of Illinois Urbana-Champaign, Champaign, IL, USA, 1979.

Disclaimer/Publisher's Note: The statements, opinions and data contained in all publications are solely those of the individual author(s) and contributor(s) and not of MDPI and/or the editor(s). MDPI and/or the editor(s) disclaim responsibility for any injury to people or property resulting from any ideas, methods, instructions or products referred to in the content.